Article

Unidirectional Crystal Orientation of Dual-Phase Ni₃Al-Based Alloy via Laser Irradiation

Satoshi Semboshi [1,*] , **Hiroshi Nakamura** [2] **, Yosuke Kawahito** [3] , **Yasuyuki Kaneno** [4]
and Takayuki Takasugi [4]

1   Institute for Materials Research, Tohoku University, Katahira 2-1-1, Aoba-ku, Sendai, Miyagi 980-8577, Japan
2   Charmant Inc., Kawasari-cho 6-8, Sabae, Fukui 916-0088, Japan; h.nakamura@charmant.co.jp
3   Advanced Science-Technology Research (ASTER) Program,
    Institute for Extra-Cutting-Edge Science and Technology Avant-Garde Research (X-Star),
    Japan Agency for Marine-Earth Science and Technology (JAMSTEC), Natsushima 2-15,
    Yokosuka 237-0061, Japan; ykawahito@jamstec.go.jp
4   Department of Materials Science, Osaka Prefecture University, Gakuen-cho 1-1, Naka-ku, Sakai,
    Osaka 599-8531, Japan; kaneno@mtr.osakafu-u.ac.jp (Y.K.); takasugi@mtr.osakafu-u.ac.jp (T.T.)
*   Correspondence: semboshi@imr.tohoku.ac.jp; Tel.: +81-22-215-2220

check for
updates

Abstract: Dual-phase Ni₃Al-based alloys feature extensive applicability even under high-temperature conditions. We selectively modified the microstructure of a representative dual-phase Ni₃Al-based alloy from equi-axed grains to unidirectional grains, using a kW-class high-power laser irradiation technique. On employing the laser probe to linearly scan the Ni-9 at.% Al-16 at.% V alloy specimen, the laser-irradiated region was partially molten and then immediately solidified from the two edges of the molten pool toward the center. Laser irradiation under low-speed scanning increased the molten pool width. The grains in the laser-irradiated region extended preferentially from the two edges toward the center; their crystal orientation was similar to adjacent substrate grains, suggesting epitaxial growth. Therefore, the unidirectional orientation of grains could be extended via wide-range scanning using laser irradiation. This suggests that the microstructure of the alloy can be selectively modified to unidirectional orientated grains by optimizing laser irradiation conditions, such as the power density, scanning speed, and scanning paths. The hardness of the laser-irradiated region decreased due to the phase transformation from the ordered Ni₃Al and Ni₃V phases to the disordered fcc phase. However, the hardness improved to a value comparable to that of the alloy subjected to heat treatment at 980 °C for 1 h.

Keywords: Ni₃Al; laser irradiation; microstructure; solidification; hardness

1. Introduction

Dual-phase Ni₃Al-based alloys composed of two different intermetallic phases, namely γ'-Ni₃Al (Strukturbericht symbol: L1₂) and γ''-Ni₃V (D0₂₂), are promising for use in high-performance components at high temperatures, such as turbine blades, engines, and friction stir welding tools [1–3]. However, these applications require materials with excellent combinations of mechanical properties, toughness, corrosion resistance, and microstructural stability at high temperatures. The expansion of the applicability of a dual-phase Ni₃Al-based alloy as a high-temperature structural material requires improved toughness and creep strength, as well as enhanced yield and tensile strengths at high temperatures. The influence of alloying transition metal elements, such as Fe, Ti, Nb, and Ta, on the mechanical properties of dual-phase Ni₃Al-based alloys has been investigated [4,5]. It was also reported that additional heat treatment of an alloy containing a small amount of Mo and W could enhance its

mechanical properties through age-induced precipitates [6]. However, from a practical perspective, preventing cracks during the fabrication and subsequent use of components still remains challenging.

To address this limitation, single crystallization or the unidirectional orientation of dual-phase Ni_3Al-based alloys should be considered. These techniques are favorable because they exhibit a significant susceptibility toward cracking at the grain boundaries transverse to the applied stress, which is similar to that observed in conventional Ni-based superalloys composed of γ-Ni (A1) and γ'-Ni_3Al ($L1_2$) [7–9]. For example, in the case of cast Ni-based superalloys, it was reported that the introduction of directionally solidified columnar grains could realize a considerable improvement in creep strength, because of a reduction in transverse grain boundaries [10]. However, in conventional techniques for directional solidification, such as slow casting and zone melting, quite small temperature gradients and extremely slow solidification rates often lead to coarse dendrite structures and considerable interdendritic segregation, eventually resulting in a significant deterioration in the mechanical performances of Ni-based superalloys. In contrast, large thermal gradients and rapid solidification processes can achieve a finer dendrite arm spacing, leading to a reduction of elemental segregation and casting defects. In addition, they are also expected to improve the mechanical properties.

High-power laser processing methods, such as laser additive manufacturing and laser re-melting [11–18], have received growing interest for use in various applications, including the building of near net shape components and the surface modification and effective repair of selected regions of Ni-based superalloys [19–21]. Moreover, the laser irradiation process can promote epitaxial crystal growth by using the appropriate parameters, and it can produce directional solidification structures due to an ultra-large temperature gradient and cooling rate during the laser process [22–24]. Actually, it was reported that a multi-pass build-up of a Ni-based superalloy (IN939) was successfully deposited on blade materials with directional solidification microstructures through laser deposition [25]. However, the application of this laser irradiation technique to dual-phase Ni_3Al-based alloys composed of brittle intermetallic phases is expected to be more challenging due to the higher cracking susceptibility. Therefore, we herein report the selective microstructure modification, from equiaxed to unidirectional orientated grains, of a representative dual-phase Ni-based alloy using a focused single-mode fiber laser with a kW-class high power density. This approach is expected to achieve a rapid cooling rate, resulting in a large temperature gradient in a narrow, but deep region.

2. Materials and Methods

According to the Ni_3Al-Ni_3V pseudo-binary phase diagram shown in Figure 1 [26], the dual-phase Ni-based alloy, composed of primary γ'-Ni_3Al ($L1_2$) and secondary γ''-Ni_3V ($D0_{22}$) phases, can be obtained by melting the specimen with a composition of Ni-(25−x) at.% Al-x at.% V (x ranges from 12 to 20), followed by annealing under the eutectoid temperature of 1000 °C. Thus, an alloy ingot with a nominal composition of Ni-9 at.% Al-16 at.% V doped with 50 ppm B was prepared, such that the composition was representative of dual-phase Ni_3Al-based alloys. A small aliquot of B was added to the ingot to suppress intergranular fractures [27–29]. A button ingot, approximately 50 mm in diameter, was fabricated via arc-melting under an Ar gas pressure of 0.1 MPa, using 99.99 wt% nickel grains, 99.9 wt% aluminum tips, 99.9 wt.% vanadium grains, and 99.9 wt.% boron powder as the raw materials. It should be noted that the chemical analysis of the constituent elements of this prepared alloy differed from the nominal compositions by less than 0.08 wt.%, indicating that an alloy of the desired composition was prepared. After arc-melting, the alloy ingot was annealed at 1050 °C for 24 h under a vacuum of less than 2×10^{-3} Pa to achieve homogenization. The ingot was then cut into sample pieces (>40 mm long, 10 mm wide, and 1.5 mm thick) using an electro-discharge machine (HS-300, Brother Industries, Ltd., Nagoya, Japan).
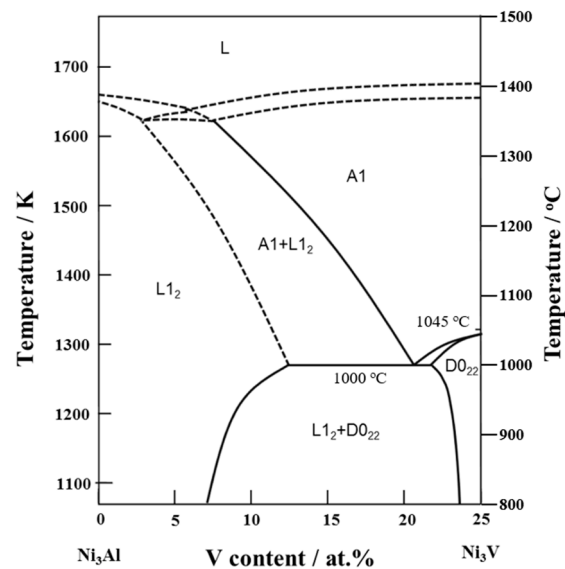
Figure 1. Ni$_3$Al–Ni$_3$V pseudo-binary phase diagram reproduced from [26], with permission from Elsevier, 2020. L1$_2$ denotes the ordered Ni$_3$Al phase, A1 the disordered face-centered cubic (fcc) phase, D0$_{22}$ the ordered Ni$_3$V phase, and L the liquid phase.

The specimen surface was ground to remove the contaminated layer using SiC abrasive paper. The specimens were irradiated with a single-mode fiber laser focused on a spot diameter of 0.054 mm with a laser output of 2 kW (corresponding to a power density of 870 kW/mm^2) under an Ar gas atmosphere. The scanning speed of the laser probe was controlled at 100, 500, 1000, and 2000 mm/s. The laser probe traveled along two paths—a line (single-path) scan of 20 mm and a wide-range (multi-path) scan; this was achieved by repeating the laser irradiation process ten times (scanning of 20 mm at 100 mm/s, stopping laser irradiation for 1 s, moving to the start point, and then shifting up by 0.05 mm), as illustrated in Figure 2. After laser irradiation, the specimens were heat treated at 980 °C for 1 h under a vacuum of <2.0 × 10^{-3} Pa, to ensure that the two phases of Ni$_3$Al and Ni$_3$V were obtained, as indicated in Figure 1.
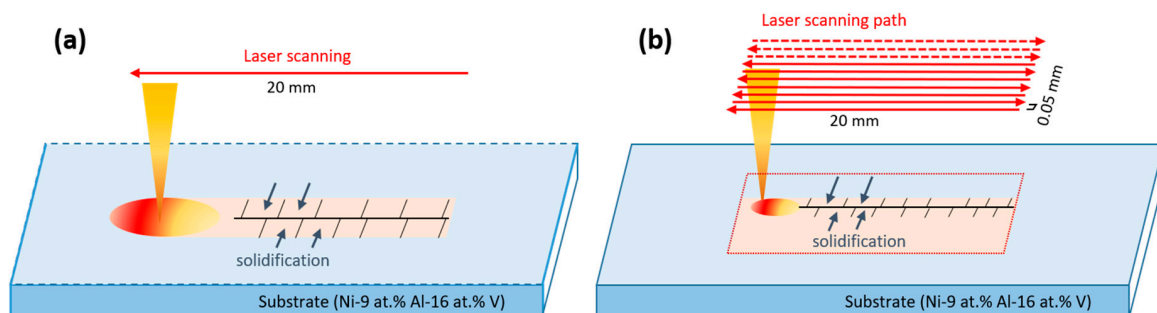

Figure 2. Illustration of the laser scanning path used for the Ni-9 at.% Al-16 at.% V alloy substrate: (**a**) line scan and (**b**) wide-range scan.

The microstructure and crystal orientation of the specimens were examined using field emission scanning electron microscopy (FESEM) (JEOL JSM-5100A, JEOL, Tokyo, Japan), equipped with an electron backscattered diffraction (EBSD) (DVC5 detector, TSL solutions, Sagamihara, Japan) apparatus operating at an acceleration voltage of 15 kV. Specimens for the FESEM observations and EBSD analyses were prepared via mechanical abrasion using SiC paper. The specimens were then electrochemically polished with a methanol solution of 15% sulfuric acid at <253 K using a voltage of 10–20 V for 30 s. Vickers hardness measurements were conducted under an applied load of 1.98 N (200 gf) for a dwell time of 10 s at a room temperature of 20 °C.

3. Results and Discussion

3.1. Single-Path Line Scanning

Figure 3 shows the micrograph of the Ni-9 at.% Al-16 at.% V alloy specimen after arc-melting and subsequent annealing at 1050 °C for 24 h. From the figure, it is evident that the microstructure of the specimen was composed of relatively large equiaxed grains, which ranged from 200 μm to 1 mm. From the magnified image, we can discern the primary fine cuboidal precipitates of $L1_2$-Ni_3Al with a size of several hundred nanometers and a channeling region of the eutectoid microstructure of the $L1_2$-Ni_3Al and $D0_{22}$-Ni_3V phases, as predicted by the Ni_3Al–Ni_3V phase diagram (Figure 1) and also by previous reports [1–4,26].
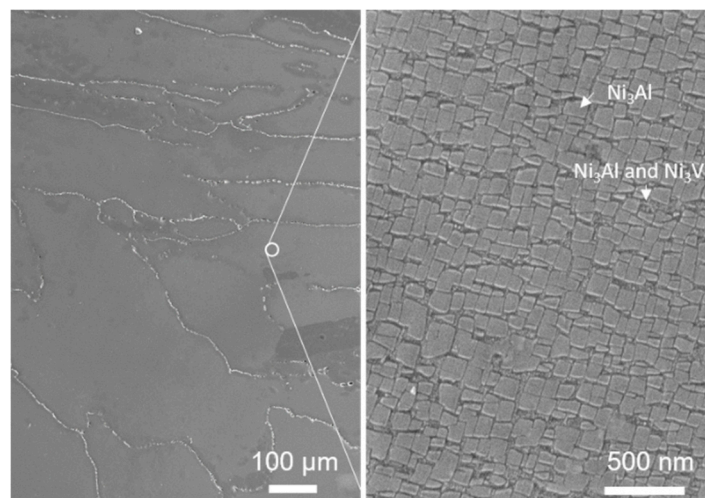

Figure 3. Field emission scanning electron microscopy (FESEM) micrograph of the Ni-9 at.% Al-16 at.% V alloy specimen after arc-melting and subsequent annealing at 1050 °C for 24 h.

Figure 4a depicts a surface FESEM image of the specimen subjected to laser irradiation via line scanning from right to left over the paper at a high speed of 2000 mm/s. We observe a linear region with a width of ~130 μm, which indicates traces of a molten pool induced due to laser irradiation. This suggests that the laser-irradiated region was locally molten and immediately solidified from the two edges of the molten pool toward the center. The width of the molten pool was wider than the laser spot diameter of 0.054 mm. The linear region contained deep-etched lines at the center, which indicate a cold shut or molten pool shrinkage due to the solidification of the molten pool from the two edges. On observing the laser-irradiated region at a higher magnification, we identified a superfine cellular interface with a spacing of approximately 1–2 μm (see the inset of Figure 4a), although no fine cuboidal particles were found (Figure 3). The morphology of the superfine cellular interface is often observed upon solidification at a significantly rapid cooling rate; this phenomenon is discussed in the concluding portion of this section.

Figure 4b,c show the inverse pole figure (IPF) map and kernel average misorientation (KAM) map obtained using EBSD analysis for the irradiated surface of the specimen by line scanning at a speed of 2000 mm/s; these maps were obtained from a different region than that in Figure 4a. The IPF map was analyzed based on the assumption that the constituent phase in the specimen was the disordered A1-fcc structure, as predicted from the phase diagram shown in Figure 1. However, it should be noted that the same IPF map was obtained even when the constituent phase was assumed to be the $L1_2$-Ni_3Al and $D0_{22}$-Ni_3V structure; this was because they were derived from an fcc structure. We found several cracks in the laser-irradiated region, as indicated in Figure 4b, and this was attributed to the sudden thermal expansion and contraction. The KAM map shown in Figure 4c, which expresses a transgranular

strain distribution by rapid solidification, also suggests that some strain was accumulated in the laser-irradiated region rather than the adjacent substrate.
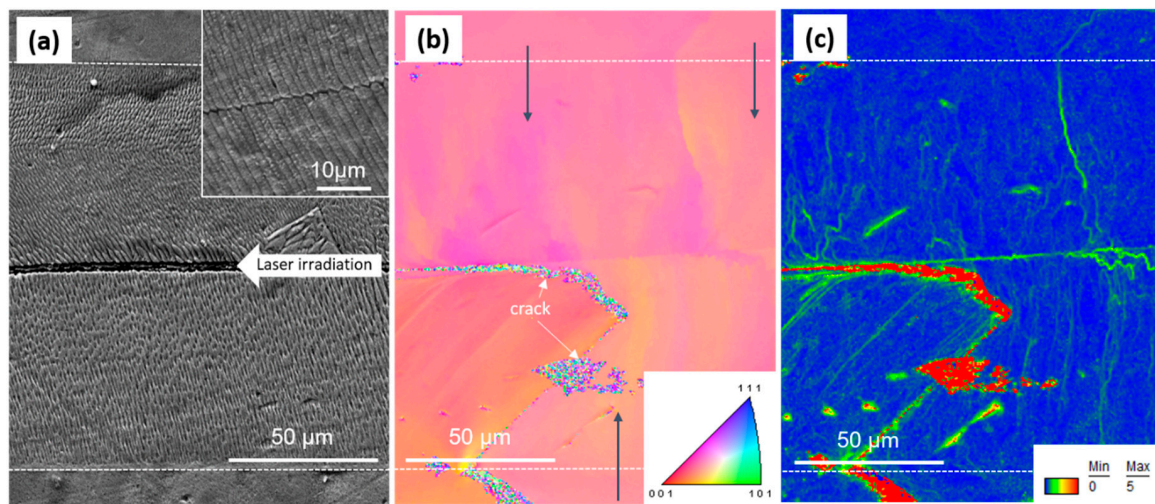

Figure 4. (**a**) Surface FESEM micrograph, (**b**) inverse pole figure (IPF) map, and (**c**) kernel average misorientation (KAM) map obtained via EBSD analysis for the Ni-9 at.% Al-16 at.% V alloy specimen linearly laser-irradiated at a scan speed of 2000 mm/s. The dotted lines indicate the interface between the substrate and traces of the molten pool. The inset in Figure 4a presents a magnified FESEM micrograph from the laser scanned region. The arrows in (**b**) indicate the solidification direction after laser scanning.

We also found from Figure 4b that the crystal grains extended preferentially in a direction perpendicular to the laser scanning direction; this was likely caused by the temperature gradient from the two edges to the center of the laser-irradiated region, as indicated by the black arrows. The crystal orientation of the grains in the laser-irradiated region was identical to that of the substrate grains adjacent to the edge of the laser-irradiated region. This suggested that the grains in the laser-irradiated region were nucleated at the molten pool adjacent to the substrate and grown epitaxially toward the center of the molten pool, thereby producing the crystal orientation of grains in the substrate that is illustrated in Figure 2a.

Figure 5a shows the surface FESEM image of the specimen irradiated by laser line scanning at a low speed of 100 mm/s. We observed linear traces of a molten pool with a width of ~650 μm, which was significantly wider than the laser spot diameter of 0.054 mm. The cracks induced during laser irradiation, as seen in the case of laser scanning at a high speed of 2000 mm/s in Figure 4b, were significantly suppressed upon decreasing the laser scan speed to 100 mm/s. In the microscopic view shown in the inset of Figure 5a, we observe fine dendrites with primary and secondary dendrite arm spacings of ~5 and 1–2 μm, respectively. Figure 5b shows an IPF map obtained via EBSD analysis of the specimen irradiated by laser line scanning at a speed of 100 mm/s. As shown, a grain extends from the edge to the center of the laser-irradiated region with the same crystal orientation as the adjacent grains in the substrate. The size of the extended grains was larger than that observed at a scan speed of 2000 mm/s, as can be seen in Figure 4.

Figure 5c,d present the cross-sectional FESEM image and IPF map of the specimen irradiated with a laser scanning speed of 100 mm/s, respectively. It appears that the laser-irradiated region completely penetrates the specimen, although the width of the region decreases from 650 μm at the surface to 500 μm at the base. We also found no macroscale defects such as pin-holes in the laser-irradiated region. Figure 5d further indicates that the grains in the laser-irradiated region have the same crystal orientation as the adjacent grains in the substrate. This demonstrates that a high power density at a laser output of 870 kW/mm^2 is sufficient to melt a Ni-9 at.% Al-16 at.% V specimen with a thickness of

1.5 mm. It should also be noted that the heat-affected zone (HAZ) between the laser-irradiated region and the substrate could not be clearly identified from the FESEM observations and EBSD analyses; this is discussed in subsequent sections.
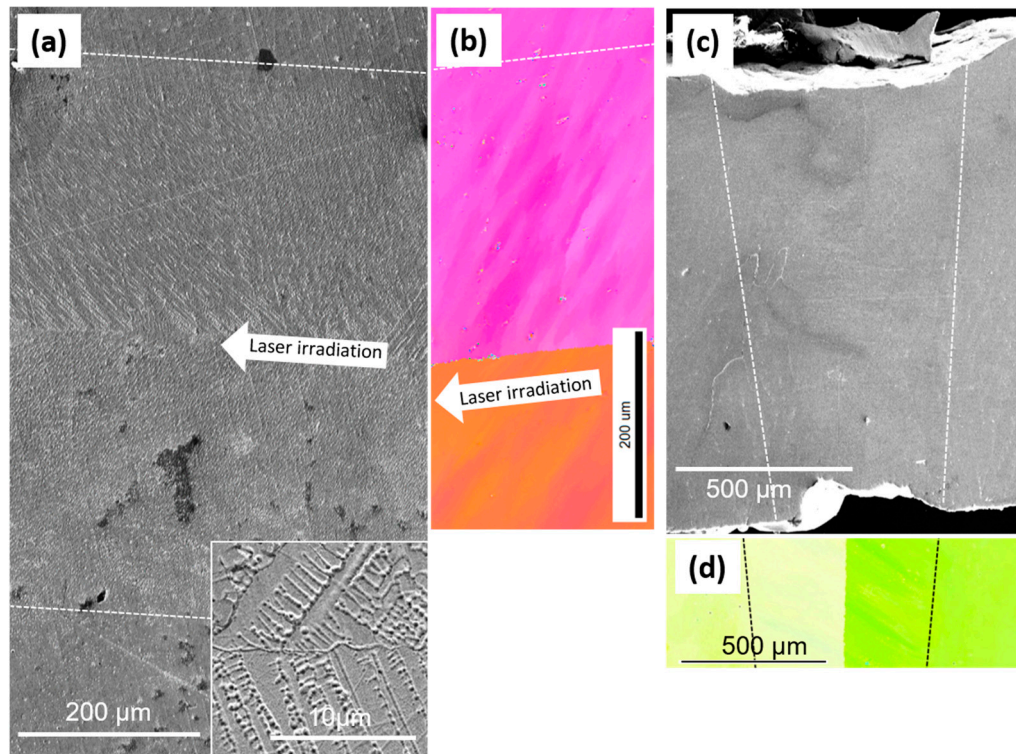

Figure 5. (**a**) Surface FESEM image and (**b**) inverse pole figure (IPF) map obtained via electron backscattered diffraction (EBSD) analysis of the Ni-9 at.% Al-16 at.% V alloy specimen irradiated linearly by a laser at a scan speed of 100 mm/s. (**c**) Cross-sectional FESEM image (**d**) and IPF map. The dotted lines indicate the interface between the substrate and traces of the molten pool.

Figure 6 shows the variation in the width of the laser-irradiated region (molten pool) in the surface at scan speeds ranging from 100 to 2000 mm/s. There was a noticeable increase in the width of the region melted by laser irradiation as the laser scan speed decreased. This can be explained by the larger heat accumulation during laser irradiation at lower scanning speeds. That is, a kW-class high-power laser irradiation at lower scanning speed should cause a more efficient laser absorption rate due to the keyhole effect. It was also confirmed that the grains for all specimens irradiated by lasers at speeds ranging from 100–2000 mm/s extended throughout the substrate to the center of the linear region, as illustrated in Figure 2a.

The cooling rate after laser-induced melting, which controlled solidification, was estimated from the cellular spacing and primary dendrite arm spacing based on previous reports on Ni_3Al-based alloys [30,31]. The cooling rate for a superfine cellular interface spacing of 5 µm (scan speed of 2000 mm/s) was estimated to be ~1×10^6 °C/s. On the contrary, the cooling rate of the primary dendrite arm spacing of ~1–2 µm (scan speed of 100 mm/s) was ~1×10^5 °C/s. Both cooling rates are considered to be extremely higher than conventional air cooling (~1×10^1 °C/s) and water quenching (~1×10^3 °C/s) rates. This high cooling rate causes a large temperature gradient between the substrate and the narrow molten pool, leading to rapid and unidirectional solidification throughout half of the linear region, followed by the formation of columnar grains. It was also observed that the cooling rate for a scan speed of 100 mm/s was lower than that for 2000 mm/s. This relatively low cooling rate corresponds to greater heat accumulation and milder thermal shrinkage upon solidification. This suppresses cracking and increases the widths of the laser-irradiated region (molten pool) in the specimen.
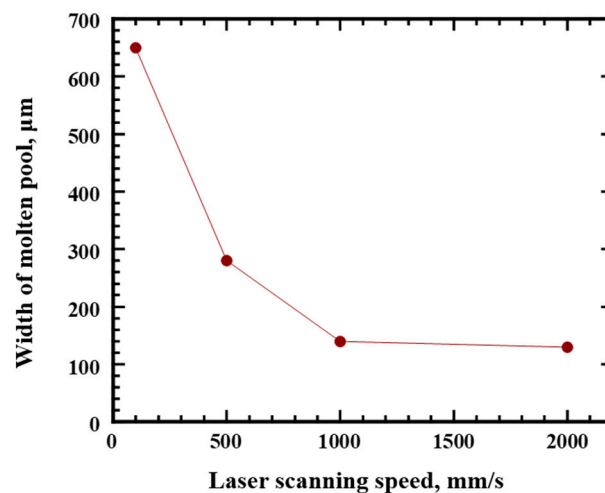
Figure 6. Variation in the width of the molten pool upon laser irradiation of the Ni-9 at.% Al-16 at.% V alloy specimen as a function of the laser scan speed.

3.2. Multi-Path Scanning

Based on previous findings, we performed a wide-range laser scan of the Ni-9 at.% Al-16 at.% V alloy specimen to demonstrate the selective microstructure modification from polycrystalline grains to unidirectional crystal-oriented grains. The surface of the specimen was laser scanned, as illustrated in Figure 2b. Figure 7 shows the FESEM image and IPF map obtained by the EBSD analysis of the wide laser-irradiated region of the specimen. Following wide-range scanning, we noticed a trace of the molten pool with dimensions of ~20 mm × 1.2 mm. Only one cold shut line was found in the center of the last linear laser scan, as indicated by the dotted line in Figure 7a. This was because the cold shut line formed in the center upon laser irradiation and disappeared when the next overlapping line scanning shifted upwards by 0.05 mm (50 µm), because the width of the laser-irradiated region was ~650 µm at a scan speed of 100 mm/s, as shown in Figures 5 and 6. Unidirectional solidified columnar grains with a length of >1.5 mm and perpendicular to the direction of laser irradiation can be seen in Figure 7b. Therefore, controlling the laser irradiation conditions, such as power density, scan speed, and scan path, facilitates the development of a unidirectionally oriented microstructures for dual-phase Ni_3Al-based alloys such as the Ni-9 at.% Al-16 at.% V alloy. If a process is established to obtain specimens with unidirectionally oriented microstructures, it must be able to produce a single crystal material. Such a process will be examined in our future research.

Figure 8 presents the line profile for Vickers hardness across the laser-irradiated regions for the specimens before and after heat treatment at 980 °C for 1 h. Before heat treating the specimen, we could observe three regions of the substrate, HAZ, and laser irradiation in the specimen, as indicated by the dotted lines in Figure 8; the Vickers hardness of the substrate for the laser-irradiated specimen was 497 ± 11 HV, which is similar to that of the specimen prior to laser irradiation. The Vickers hardness decreased to ~402 HV in the laser-irradiated region with a width of ~1.2 mm. However, after heat treatment at 980 °C for 1 h, the Vickers hardness for the regions with and without laser irradiation was 570 ± 6 and 568 ± 5 HV, respectively, indicating a relatively insignificant difference between the two regions.

The decrease and increase in the Vickers hardness upon laser irradiation and heat treatment, respectively, are attributed to microstructural transformations. Prior to laser irradiation, the grains in the specimen consisted of primary fine cuboidal particles of $L1_2$-Ni_3Al and a channeling region of the eutectoid microstructure of the $L1_2$-Ni_3Al and $D0_{22}$-Ni_3V phases, as shown in Figure 1. After laser irradiation, the molten region solidified from the liquid phase at a significantly high cooling rate. This high cooling rate potentially leads to the formation of a disordered A1-fcc phase in the grains (Figure 1) and eventually degrades strength. However, the microstructure can be modified again to

yield fine dual-phases of $L1_2$-Ni_3Al and $D0_{22}$-Ni_3V via heat treatment at 980 °C for 1 h, which results in the recovery and improvement of mechanical properties.
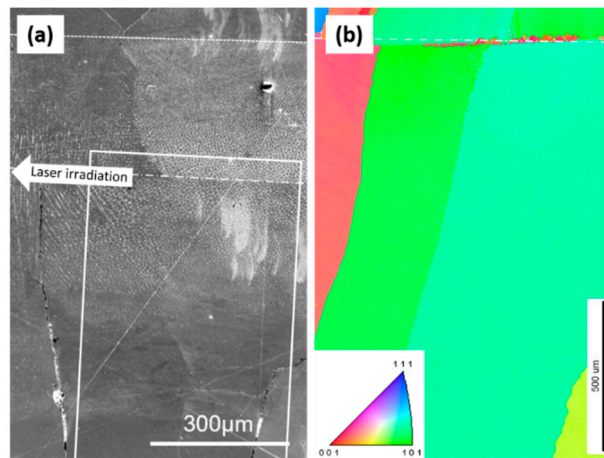

Figure 7. (**a**) Surface FESEM image and (**b**) inverse pole figure (IPF) map obtained by the EBSD analysis of the Ni-9 at.% Al-16 at.% V alloy specimen with a wide laser-irradiated region at a scan speed of 100 mm/s. The IPF map was measured from the laser-irradiated region, as indicated by the solid square in (**a**). The dotted and dashed-and-dotted lines indicate the interface between the substrate and traces of the molten pool, and the cold shut, respectively.
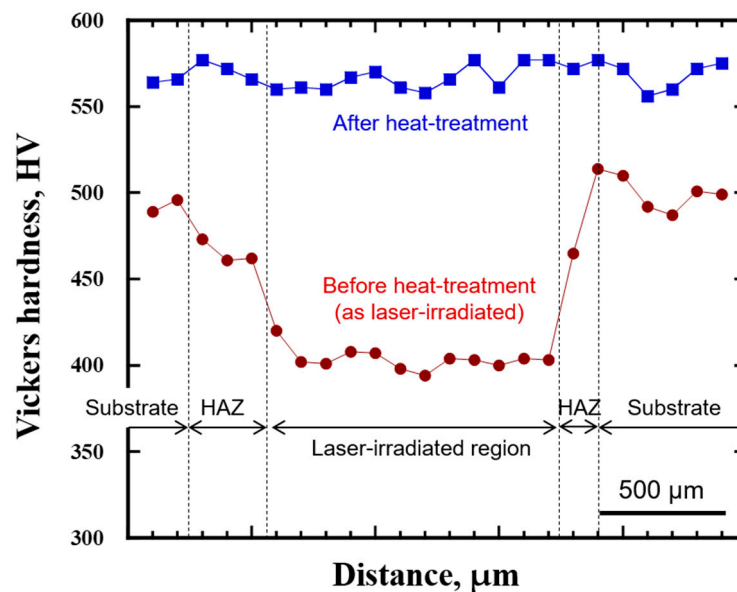

Figure 8. Vickers hardness line profile across the laser-irradiated region of the Ni-9 at.% Al-16 at.% V alloy specimens before and after heat treatment at 980 °C for 1 h.

Thus, it was herein demonstrated that a combination of laser processing and heat treatment could be considered as a promising technique to control the microstructure of the alloy and improve its properties. Furthermore, it is expected that the findings obtained in this paper are useful not only for modifying and repairing the partial microstructure of the alloy, but also for controlling the alloy microstructure in the field of laser additive manufacturing techniques.

4. Conclusions

We herein reported our examination of the variations in the microstructure and mechanical properties of a representative dual-phase Ni-based alloy irradiated by a powerful single-mode fiber

laser with a power density of 870 kW/mm^2 at a scan speed of 100–2000 mm/s. The Ni-9 at.% Al-16 at.% V alloy specimen was partially molten when subjected to line laser scanning and then immediately solidified from the two interfaces between the substrate and the molten pool to the center. The width of the molten pool increased as the laser scan speed decreased. Given the large temperature gradient between the substrate and the molten pool, rapid and unidirectional solidification occurred in half of the linear region. The crystal orientation of the grains in the laser-irradiated region was identical to that adjacent to the substrate grains. Based on the above findings, it can be proposed that wide-range laser scanning is suitable for the partial modification of the microstructure from equiaxed grains to unidirectional orientated grains. The hardness of the specimen was found to reduce upon laser irradiation due to the microstructural transformation from the ordered L1$_2$-Ni$_3$Al and D0$_{22}$-Ni$_3$V phases to a disordered A1-fcc phase. However, the hardness was recovered and improved via heat treatment at 980 °C for 1 h, which was comparable with the hardness of the substrate Ni-9 at.% Al-16 at.% V alloy. Thus, optimized laser irradiation is a promising technique for modifying the microstructure and mechanical properties of the surface and selective regions of dual-phase Ni$_3$Al-based alloys.

Author Contributions: Conceptualization, S.S.; methodology, S.S., H.N., and Y.K. (Yosuke Kawahito); sample preparation, H.N.; validation, Y.K. (Yasuyuki Kaneno) and T.T.; formal analysis, S.S.; investigation, S.S.; resources, S.S.; data curation, S.S.; writing, original draft preparation, S.S.; writing, review, and editing, Y.K. (Yasuyuki Kaneno) and T.T.; supervision, T.T. All authors have read and agreed to the published version of the manuscript.

Conflicts of Interest: The authors declare no conflict of interest.

References

1. Nunomura, Y.; Kaneno, Y.; Tsuda, H.; Takasugi, T. Phase relation and microstructure in multi-phase intermetallic alloys based on Ni$_3$Al-Ni$_3$Ti-Ni$_3$V pseudo-ternary alloy system. *Intermetallics* **2004**, *12*, 389–399. [CrossRef]

2. Shibuya, S.; Kaneno, Y.; Yoshida, M.; Takasugi, T. Dual multi-phase intermetallic alloys composed of geometrically close packed Ni$_3$X (X: Al, Ti and V) type structures-II. Mechanical properties. *Acta Mater.* **2006**, *54*, 861–870. [CrossRef]

3. Kawahara, K.; Kaneno, Y.; Kakitsuji, A.; Takasugi, T. Microstructural factors affecting hardness property of dual two-phase intermetallic alloys based on Ni$_3$Al-Ni$_3$V pseudo-binary alloy system. *Intermetallics* **2009**, *17*, 938–944. [CrossRef]

4. Ioroi, K.; Kaneno, Y.; Semboshi, S.; Takasugi, T. Effect of transition metal addition on microstructure and hardening behavior of two-phase Ni$_3$Al-Ni$_3$V intermetallic alloys. *Materialia* **2019**, *5*, 100173. [CrossRef]

5. Kato, H.; Semboshi, S.; Kaneno, Y.; Takasugi, T. Effects of Iron Addition on the Microstructures and Mechanical Properties of Two-Phase Ni$_3$Al-Ni$_3$V Intermetallic Alloys. *Metall. Mater. Trans. A* **2020**, *51*, 2469–2479. [CrossRef]

6. Edatsugi, D.; Kaneno, Y.; Semboshi, S.; Takasugi, T. Fine precipitation in channel region of two-phase Ni$_3$Al and Ni$_3$V intermetallic alloys containing Mo and W. *Metall. Mater. Trans. A* **2016**, *47A*, 998–1008. [CrossRef]

7. Liu, C.T. Intergranular fracture and boron effects in Ni$_3$Al and other intermetallics—Introductory paper. *Scr. Metall. Mater.* **1991**, *25*, 1231–1236. [CrossRef]

8. Lin, H.; Pope, D.P. The influence of grain boundary geometry on intergranular crack propagation in Ni$_3$Al. *Acta Metall. Mater.* **1993**, *41*, 553–562. [CrossRef]

9. Xie, G.; Wang, L.; Zhang, J.; Lou, L.H. Orientational dependence of recrystallization in an Ni-base single-crystal superalloy. *Scr. Metall.* **2012**, *66*, 378–381. [CrossRef]

10. Yang, F.; Wang, J.; Yu, J.; Zhou, Z.; Wang, B.; Tu, T.; Ren, X.; Deng, K.; Ren, Z. Microstructure and mechanical properties of Ni-based superalloy K418 produced by the continuous unidirectional solidification process. *J. Mater. Eng. Perform.* **2019**, *28*, 6483–6491. [CrossRef]

11. Gaumann, M.; Bezencon, C.; Canalis, P.; Kurz, W. Single-crystal laser deposition of superalloys: Processing-microstructure maps. *Acta Mater.* **2001**, *49*, 1051–1062. [CrossRef]

12. Haranzhevskiya, E.V.; Danilovc, D.A.; Krivilyova, M.D.; Galenkob, P.K. Structure and mechanical properties of structural steel in laser resolidification processing. *Mater. Sci. Eng. A* **2004**, *375–377*, 502–506. [CrossRef]

13. Weiping, L.; DuPont, J.N. Direct Laser Deposition of a Single-Crystal Ni_3Al-Based IC221W Alloy. *Metall. Mater. Trans. A* **2005**, *36A*, 3397–3406.

14. Ding, R.G.; Ojo, O.A.; Chaturvedi, M.C. Laser beam weld-metal microstructure in a yttrium modified directionally solidified Ni_3Al-base alloy. *Intermetallics* **2007**, *15*, 1504–1510. [CrossRef]

15. Martin, J.H.; Yahata, B.D.; Hundley, J.M.; Mayer, J.A.; Schaedler, T.A.; Pollock, T.M. 3D printing of high-strength aluminium alloys. *Nature* **2017**, *549*, 365–369. [CrossRef]

16. Godec, M.; Podgornik, B.; Nolan, D. Microstructural Development in a Laser-Remelted Al-Zn-Si-Mg Coating. *Sci. Rep.* **2017**, *7*, 16097. [CrossRef]

17. Seede, R.; Shoukr, D.; Zhang, B.; Whitt, A.; Gibbons, S.; Flater, P.; Elwany, A.; Arroyave, R.; Karaman, I. An ultra-high strength martensitic steel fabricated using selective laser melting additive manufacturing: Densification, microstructure, and mechanical properties. *Acta Mater.* **2020**, *186*, 199–214. [CrossRef]

18. Bajaj, P.; Hariharan, H.; Kini, A.; Kurnsteiner, P.; Raabe, D.; Jagle, E.A. Steels in additive manufacturing: A review of their microstructure and properties. *Mater. Sci. Eng. A* **2020**, *772*, 138633. [CrossRef]

19. Zhong, M.; Sun, H.; Liu, W.; Zhu, X.; He, J. Boundary liquation and interface cracking characterization in laser deposition of Inconel 738 on directionally solidified Ni-based superalloy. *Scr. Mater.* **2005**, *53*, 159–164. [CrossRef]

20. Lin, X.; Yue, T.M.; Yang, H.O.; Huang, W.D. Microstructure and phase evolution in laser rapid forming of a functionally graded Ti-Rene88DT alloy. *Acta Mater.* **2006**, *54*, 1901–1915. [CrossRef]

21. Lapin, J.; Marecek, C. Effect of growth rate on microstructure and mechanical properties of directionally solidified multiphase intermetallic Ni-Al-Cr-Ta-Mo-Zr. *Intermetallics* **2006**, *14*, 1339–1344. [CrossRef]

22. Li, J.; Wang, H.M. Microstructure and mechanical properties of rapid directionally solidified Ni-base superalloy Rene'41 by laser melting deposition manufacturing. *Mater. Sci. Eng. A* **2010**, *527*, 4823–4829. [CrossRef]

23. Cia, S.; Lianga, J.; Li, J.; Zhoua, Y.; Sun, Y. Microstructure and tensile properties of DD32 single crystal Ni-base superalloy repaired by laser metal forming. *J. Mater. Sci. Technol.* **2020**, *45*, 23–34. [CrossRef]

24. Vilar, R.; Santos, E.C.; Ferreira, P.N.; Franco, N.; Silva, R.C. Structure of NiCrAlY coatings deposited on single-crystal alloy turbine blade material by laser cladding. *Acta Mater.* **2009**, *57*, 5292–5302. [CrossRef]

25. Sexton, L.; Lavin, S.; Byrne, G.; Kennedy, A. Laser cladding of aerospace materials. *J. Mater. Proc. Technol.* **2002**, *122*, 63–68. [CrossRef]

26. Kobayashi, S.; Sato, K.; Hayashi, E.; Osaka, T.; Konno, T.J.; Kaneno, Y.; Takasugi, T. Alloying effects on the phase equilibria among $Ni(A1)$, $Ni_3Al(L1_2)$ and $Ni_3V(D0_{22})$ phases. *Intermetallics* **2012**, *23*, 68–75. [CrossRef]

27. Aoki, K. Ductilization of $L1_2$ intermetallic compound Ni_3Al by microalloying with boron. *Mater. Trans. JIM* **1990**, *31*, 443–448. [CrossRef]

28. Liu, C.T.; White, C.L.; Horton, J.A. Effect of boron on grain-boundaries in Ni_3Al. *Acta Metall.* **1985**, *33*, 213–229. [CrossRef]

29. Muller, D.A.; Subramanian, S.; Batson, P.E.; Silcox, J.; Sass, S.L. Structure, chemistry and bonding at grain boundaries in Ni_3Al—I. The role of boron in ductilizing grain boundaries. *Acta Mater.* **1996**, *44*, 1637–1645. [CrossRef]

30. Kim, H.K.; Earthman, J.C.; Lavernia, E.J. Primary dendrite arm spacings and tip radii in directionally solidified Ni_3Al. *Mater. Sci. Eng. A* **1992**, *152*, 240–246. [CrossRef]

31. Zhang, Y.; Huang, B.; Li, J. Microstructural evolution with a wide range of solidification cooling rates in a Ni-based superalloy. *Metall. Mater. Trans. A* **2013**, *44A*, 1641–1644. [CrossRef]